Lasing Dynamics of Optically-Pumped Ultralow-Threshold Raman Silicon Nanocavity Lasers

Daiki Yamashita,[1,][*] Yasushi Takahashi,[1] Jun Kurihara,[1] Takashi Asano,[2] and Susumu Noda[2,3]

[1]*Department of Physics and Electronics, Osaka Prefecture University, Sakai, Osaka 599-8570, Japan*
[2]*Department of Electronic Science and Engineering, Kyoto University, Kyoto 615-8510, Japan*
[3]*Photonics and Electronics Science and Engineering Center, Kyoto University, Kyoto 615-8510, Japan*

We investigate the lasing dynamics of optically-pumped submicrowatt-threshold Raman silicon lasers that employ a high-quality (high-Q) nanocavity design. The measurements reveal that free carriers generated by two-photon absorption induce dynamic effects during the initial lasing process, even at the very low threshold power of 0.12 μW. At higher excitation powers, the Raman laser signal exhibits a significant reduction within a few hundred nanoseconds after the initial rise, followed by clear oscillations. We find that the temporal behavior of the laser signal strongly depends on the excitation wavelength. However, the Raman laser signal converges to a stable continuous operation within a few microseconds after the initial rise for any excitation power employed in this work. Numerical simulations indicate that the oscillations reflect the dynamic shift of the resonant wavelength due to the thermo-optic effect and the carrier-plasma effect, which are induced by free carriers generated via two-photon absorption. These results are useful for understanding the correct design of future devices that employ Raman silicon nanocavity lasers.

I. INTRODUCTION

The development of silicon (Si)-based lasers has been very challenging during the last half century, because Si has an indirect band gap, which results in very low gain factors [1,2]. To solve the problem of the lack of optical gain in bulk crystalline Si, the use of stimulated Raman scattering (SRS) has been proposed [3–12]. Since Raman Si lasers enable continuous-wave (cw) operation at room temperature in the telecommunication wavelength regime [13–15], they are attractive for information technologies. We have developed a Raman Si laser based on a high-quality- (high-Q)-factor photonic-crystal (PC) nanocavity with a resonator size of 10 μm that enables an ultralow threshold of approximately 1 μW [16,17]. Such a small, low-threshold device is suited for dense integration on Si photonic circuits, which can be employed for applications such as cw laser sources and all-optical switching devices. However, the optical responses of the cavity need to be investigated before a suitable device structure can be designed. In particular, it is important to study the lasing dynamics with time-domain measurements to obtain information about initial lasing behavior, lasing stability, and carrier dynamics.

It is known that the output of the Raman Si laser tends to saturate for increasing excitation power because of free-carrier absorption (FCA). In high-Q cavity structures,

free carriers can be easily generated via two-photon absorption (TPA) of incident light with energy less than the band gap of Si. The resulting free carriers induce loss by additional absorption. The effects of FCA on the laser performance have been intensively studied for Raman Si lasers that employ racetrack and Fabry-Perot cavities consisting of rib waveguides [18–21]. Compared to the abovementioned device structures, the SRS and other nonlinear optical effects are significantly enhanced in Raman Si lasers based on high-Q nanocavities, because the mode volumes of the nanocavities are about 4 orders of magnitude smaller [22–24]. Various dynamic effects that are induced by the thermo-optic effect, the carrier-plasma effect, and the Kerr effect have been reported for high-Q Si nanocavities [25–27]. They originate from TPA carriers and may affect the Raman lasing dynamics. Furthermore, such nanocavities have carrier lifetimes of about 1 ns [28,29], which is more than ten times shorter than those of cavities based on rib waveguides [12,14]. The short lifetime is a result of a high surface recombination rate due to the large ratio between the surface area and volume of the nanocavity. Therefore, the magnitude of the influence of TPA carriers on the laser performance should be different from that for the rib-waveguide Raman Si lasers.

In this work, we perform time-domain measurements on ultralow-threshold Raman Si nanocavity lasers. Our measurements reveal that the various nonlinear effects induced by TPA carriers determine the initial lasing dynamics even at low excitation powers. At high excitation powers, the

[*]d-yamashita@pe.osakafu-u.ac.jp

laser signal shows a significant reduction after the initial rise and exhibits large oscillations in the following. These experimental results are well explained by the shift of the resonance peak caused by the thermo-optic effect and the carrier-plasma effect that accompany the TPA. Although the laser dynamics and the output strongly depend on the excitation wavelength, it is demonstrated that the Raman laser signal converges to a stable continuous operation for any excitation condition employed in this work.

II. SAMPLE STRUCTURE AND EXPERIMENTAL METHOD

The nanocavity-based Raman Si laser utilizes two high-Q nanocavity modes to confine the pump light and the Stokes Raman scattered light. Figure 1(a) shows a schematic of the heterostructure nanocavity utilized for the Raman laser, which is formed by the line defect of air holes [24]. The distance (a) between the air holes in the x direction is increased in steps of 5 nm, with the largest distance being at the center. The wider air-hole distance locally increases the effective refractive index and thus lowers the resonance frequencies of the two propagation bands in the line defect [Fig. 1(b); formation of a multi-heterostructure]. As a result, the two high-Q nanocavity modes are formed by the confinement [17]. We utilize the nanocavity mode arising from the second propagation band (blue) to confine the pump laser light and the mode arising from the first propagation band (red) to confine the Stokes Raman scattered light. They will hereafter be referred to as the pump mode and the Stokes mode, respectively. Figures 1(c) and 1(d) show the calculated y components of the electric field distributions of the pump mode ($E_{y,\text{pump}}$) and the Stokes mode ($E_{y,\text{Stokes}}$), respectively. Each distribution is normalized by its maximum electric field value.

We fabricate the Raman laser on a (100) Si-on-insulator (SOI) substrate, which has a top Si layer thickness of 220 nm and a buried-oxide (BOX) layer thickness of 3 μm. By removing the BOX layer underneath the PC-patterned region we obtain an air-suspended structure. In order to enhance the Raman gain, the x direction of the nanocavity is chosen along the [100] crystalline direction of the substrate and the air-hole radius is set to about 130 nm to obtain a frequency spacing (Δf) of nearly 15.606 THz between the two modes, which is the Raman shift of Si nanocavities. We experimentally and numerically confirm that Δf can be tuned to the Raman shift by varying the air-hole radius with a rate of 0.15 THz/nm [13]. We fabricate several cavities with different hole radii with 0.3 nm spacing on the same chip and use the cavities with Δf close to 15.606 THz. Further details of the laser structure, the fabrication procedure, and the Raman shift can be found in previous reports [16,17,30]. The theoretical Q factor for the pump mode ($Q_{p,\text{theory}}$) calculated by the three-dimensional (3D) finite-difference time-domain
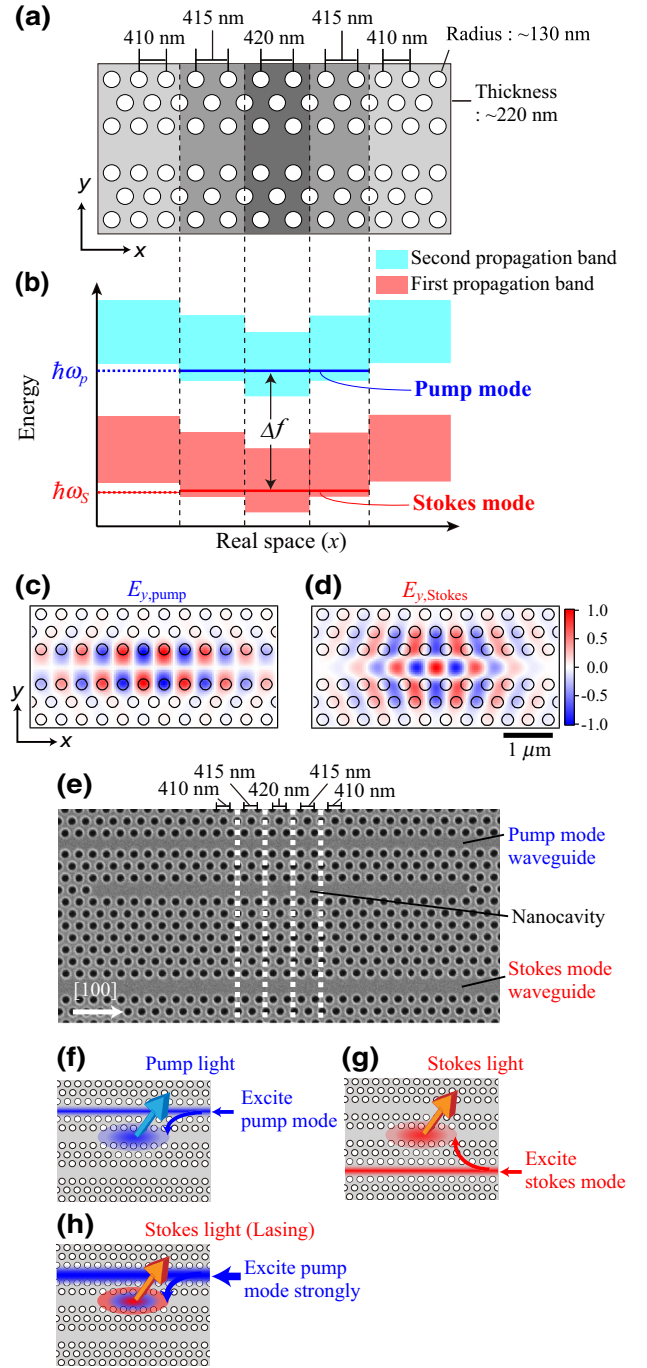

FIG. 1.   (a) Schematic of the heterostructure nanocavity used for the Raman laser. (b) Band diagram of the nanocavity. The pump nanocavity mode and Stokes nanocavity mode arise from the two propagation bands. White areas present the mode gap frequency regions. (c) Calculated electric field distributions for the pump nanocavity mode and (d) the Stokes nanocavity mode. The color scale represents the normalized intensity of the electric field. (e) SEM top view of the core region of one fabricated sample. The x direction is along the [100] crystalline direction of the (100) SOI wafer. (f–h) Nanocavity under different excitation conditions to measure the properties of (f) the pump mode, (g) the Stokes mode, and (h) the Raman laser. A long (short)-pass filter is used to measure the Raman (pump) emission.

(FDTD) method is 5.40×10^5 and that for the Stokes mode ($Q_{S,\text{theory}}$) is 5.50×10^6. The form of E_y in the x direction should slowly vary in order to increase the Q_{theory} [23,24]. As shown in Figs. 1(c) and 1(d), the distribution of $E_{y,\text{pump}}$ is closer to the air holes than that of $E_{y,\text{Stokes}}$ and therefore the form of $E_{y,\text{pump}}$ along the x direction tends to deviate from a gentle envelope function (Gaussian curve), which results in a low $Q_{p,\text{theory}}$ when compared with $Q_{S,\text{theory}}$.

Figure 1(e) is a scanning electron microscopy (SEM) image of one fabricated sample. It can be seen that the actual samples additionally contain two excitation waveguides that are fabricated parallel to the cavity. Figures 1(f)–1(h) illustrate the different measurement configurations for the pump- and Stokes-mode excitations used in the experiments. To measure the optical properties of the pump mode, the sample is excited through the pump excitation waveguide using an external tunable laser (SANTEC, TSL-510) and the light emitted from the cavity in the direction vertical to the slab is detected as shown in Fig. 1(f). Figure 1(g) shows the configuration that enables measurement of the properties of the Stokes mode. Figure 1(h) is essentially the same as Fig. 1(f), but illustrates the Raman laser operation when the pump mode is strongly excited. When we measure the emission from the Stokes (pump) mode under laser operation, a long (short) pass filter with a cutoff wavelength of 1500 nm is inserted.

For the time-domain measurement, the samples are placed in an isolation chamber in order to reduce the temperature fluctuation. An electro-optical modulator produced rectangular excitation pulses, which are incident to the facets of the excitation waveguides. The time evolution of the emission from the nanocavity modes is measured by a photomultiplier tube (Hamamatsu Photonics, H10330A-75) using the time-correlated single-photon counting (TCSPC) method. Each signal is integrated for 1 (in Sec. IV) or 3 (in Sec. V) minutes to assure a low measurement error. Further details of this measurement technique can be found in the literature [31,32].

III. SAMPLE CHARACTERIZATION

We utilize two laser samples (called A and B) for the time-domain measurements. Table I shows that the Q_p and Q_S of sample A are larger than those of sample B. In this section, we investigate their optical properties under cw excitation. In Sec. IV we discuss the time evolution of the cavity emission from sample A under excitation with intensities close to the threshold power (I_{th}). The TPA-induced effects can be easily observed in sample A even at I_{th} due to the high Q. In Sec. V, the temporal response from sample B under a high input power corresponding to $8 \times I_{\text{th}}$ is analyzed. As described later, the dynamic shift of the resonant wavelength induced by TPA carriers is significant for high input powers. The low Q_p of sample B is

TABLE I. Parameters of the laser samples.

Parameter	Sample A	Sample B
λ_p (nm)	1417.7128	1423.9480
λ_S (nm)	1530.6631	1538.0479
Δf (THz)	15.600	15.614
Q_p	4.01×10^5	1.66×10^5
Q_S	2.35×10^6	1.59×10^6
Threshold (nW)	120	440
Efficiency (%)	24.1	13.8

adequate to investigate the lasing dynamics in the strong excitation regime with high reproducibility.

Figure 2 shows the optical properties of the two Raman laser samples obtained under cw excitation. The details of the cw measurement technique can be found in our previous publication [33]. Figures 2(a) and 2(b) show the resonant emission spectra from sample A for the pump mode and the Stokes mode, respectively. A sufficiently low excitation power of 5 nW is chosen to avoid influences from TPA. The Q values for the pump mode (Q_p) including the influence of the coupled excitation waveguides can be estimated from the resonant wavelengths (λ_0) and the linewidths ($\Delta\lambda$) according to the definition $Q = \lambda_0/\Delta\lambda$. To obtain the Q for the Stokes mode (Q_S) with a value larger than 2 million, we employed a time-domain measurement, which is described in the next section. For sample A, we find $Q_p = 4.01 \times 10^5$ and $Q_S = 2.35 \times 10^6$. These values are larger than those for the Raman laser that has previously been reported [16]. The Δf of the two modes is 15.600 THz, which is very close to the Raman shift of the
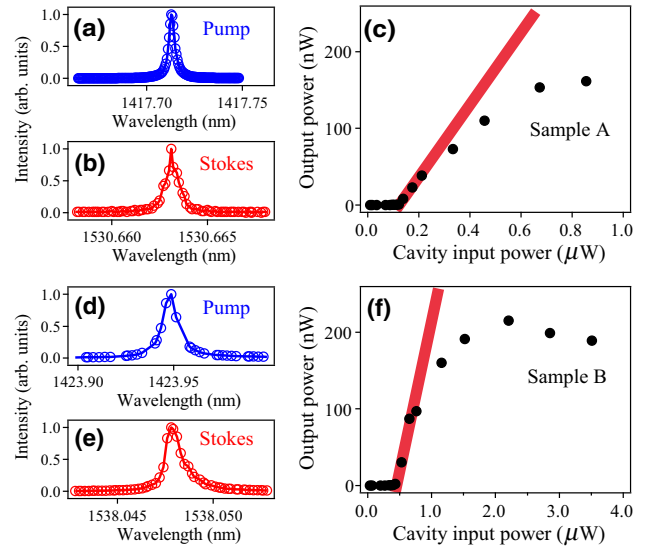

FIG. 2. Resonant spectra of (a) the pump nanocavity mode, (b) the Stokes nanocavity mode, and (c) laser output power as a function of pump power coupled into the nanocavity for sample A. (d–f) Results for sample B.

Si nanocavities [30]. Figure 2(c) shows the input/output characteristic of sample A for excitation of the pump mode with the cw laser. The x axis represents the power coupled into the pump mode (P_{input}) while the y axis is the Stokes Raman output power (P_{output}). The threshold power is 120 nW and the maximum efficiency of 24.1%. This exceptional performance is possible because of the high Q factors of the two nanocavity modes and a very small detuning between Δf and the Raman shift.

Figures 2(d) and 2(e) show the resonant emission spectra from sample B for the pump mode and the Stokes mode, respectively. For this sample we find $Q_p = 1.66 \times 10^5$, $Q_S = 1.59 \times 10^6$, and $\Delta f = 15.614$ THz. Figure 2(f) shows the input/output characteristic of sample B. The threshold power is 440 nW, which is higher than that of sample A. The maximum efficiency is 13.8%, which is significantly lower because of the lower Q values and the larger detuning.

We note that the measured Q values are lower than the Q_{theory} because the radii and positions of the air holes in the sample vary randomly on a subnanometer scale [34]. The P_{input} and P_{output} for Figs. 2(c) and 2(f) are estimated

from the light emission intensities of the corresponding nanocavity modes as illustrated in Fig. 1(h). Because the collection efficiency of the emitted light varies for each sample due to the random air-hole variations, the estimated powers should include some error [34]. We also note that P_{output} depends on the excitation wavelength. When obtaining the data in Figs. 2(c) and 2(f), the excitation laser is tuned for each measurement point to the wavelength where P_{output} is maximized. The optimum wavelength for the maximum P_{output} is slightly unstable due to various experimental fluctuations. Because of these uncertainties, a quantitative comparison between Figs. 2(c) and 2(f) and other data is not considered appropriate.

IV. TIME-DOMAIN MEASUREMENTS CLOSE TO THE THRESHOLD

Figures 3(a) and 3(b) show the time evolution of the emission from the pump mode and the Stokes mode, respectively, for Sample A under pulsed excitation of the pump mode. The experimental configuration is shown in Fig. 1(h). For this measurement the excitation wavelength
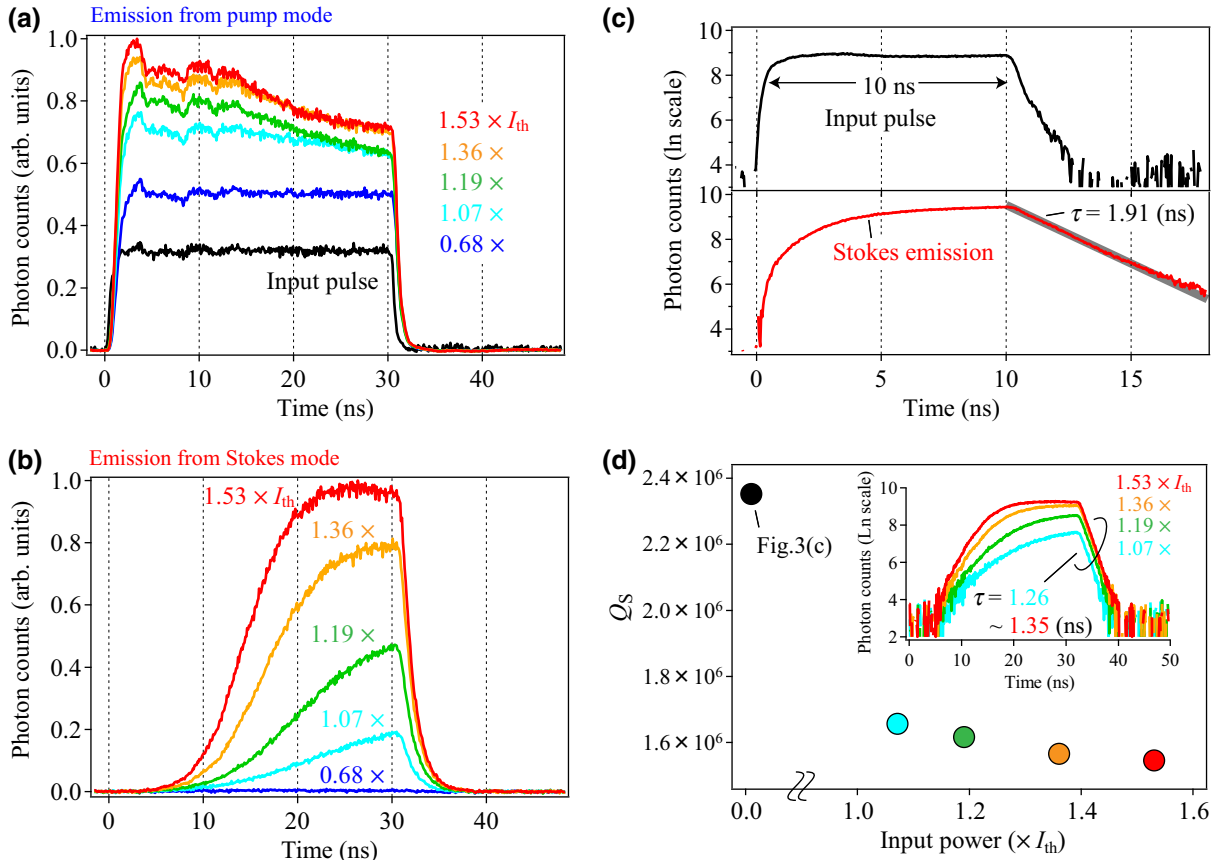

FIG. 3.   (a) Time-resolved signals of the pump mode and (b) the Stokes mode under Raman laser operation with various P_{input}. P_{input} is normalized by I_{th}. The excitation wavelength is set to λ_p. (c) Time-resolved signals of input pulse (black curve) and Stokes light (red curve) when the Stokes mode waveguide is excited. (d) Dependence of Q_S on P_{input} under Raman laser operation. The x axis is normalized by I_{th}. The inset shows the time-resolved signals of Fig. 3(b) in a logarithmic scale.

is set to λ_p, which is the intrinsic resonance wavelength of the pump mode presented in Table I. The measurements for the pump mode and the Stokes mode are performed for various P_{input}. For excitation, a pulsed light with a temporal width of 30 ns and a repetition rate of 2 MHz is used. The slow repetition rate is required to suppress any possible pile-up effect that can be induced by the TPA carriers. The origin of the x axis indicates the start of the excitation pulse. The black line in Fig. 3(a) shows the scattered light at the facet of the waveguide, which represents the shape of the input pulse.

For $P_{\text{input}} = 0.68 \times I_{\text{th}}$, we observe a sharp initial rise of the pump mode emission [Fig. 3(a); dark blue curve] at the start of the excitation pulse and then the intensity is constant until 30 ns, while the Stokes signal is almost zero [Fig. 3(b); dark blue curve]. For $P_{\text{input}} = 1.07 \times I_{\text{th}}$, the pump signal slowly decreases between 10 and 30 ns [Fig. 3(a); light blue curve] while the Stokes signal [Fig. 3(b); light blue curve] starts to increase for times later than 10 ns. These opposite responses clearly indicate the wavelength conversion by SRS. For a higher P_{input}, the slope of the initial rise for the Stokes signal increases because the Raman gain increases. The Stokes signal for $P_{\text{input}} = 1.07 \times I_{\text{th}}$ shows no saturation at 30 ns. It reaches its maximum intensity at 25 ns for $P_{\text{input}} = 1.53 \times I_{\text{th}}$ and between 25 and 30 ns the signal decreases slightly. This reduction is due to the wavelength shift of the pump mode, which is described in Secs. V and VI.

It is noted that for any excitation power the Stokes signal in Fig. 3(b) rises a few nanoseconds after the input pulse. This delayed onset mainly originates from the high Q_S value of more than a million. In fact, the initial rise of the pump mode shown in Fig. 3(a) is also slightly delayed from that of the input pulse due to the Q_p of 4.01×10^5.

It is important to note that for times later than 30 ns, after the pump light is switched off, the Stokes signals decay slowly as shown in Fig. 3(b). These decays reflect the Q_S values including the losses through TPA-induced FCA [18–21]. Therefore, a comparison between these values and the intrinsic Q_S value enables a prediction of the magnitude of the FCA influence [35]. Figure 3(c) shows the experimental result from which the intrinsic Q_S is determined. The Stokes mode is directly excited at λ_S with a low input power ($<0.04 \times I_{\text{th}}$) as illustrated in Fig. 1(g). The input pulse is set to a width of 10 ns and a repetition rate of 10 MHz is used. The black curve shows the input pulse signal in a logarithmic scale. After 10 ns, a fast decay with a time constant of 370 ps can be observed, which is the time resolution of the system. The red curve represents the signal of the Stokes mode, and the photon lifetime (τ) estimated from the decay for times later than 10 ns is 1.91 ns. Thus, the intrinsic value of Q_S is estimated to be 2.35×10^6 according to the relationship $Q = \omega\tau$, where ω is the angular frequency.

Figure 3(d) shows the dependence of Q_S on P_{input} under Raman laser operation. The inset shows the data of Fig. 3(b) on a logarithmic scale to clarify the difference of the decays after 30 ns. We estimate the Q_S values from the photon lifetimes that are obtained from the decays between 33 and 35 ns (the photon lifetimes are slightly overestimated since the signal is convoluted with the carrier lifetime of the Si nanocavity, which is about 1 ns [28,29]). We find that the Q_S is reduced to 1.66×10^6 at $P_{\text{input}} = 1.07 \times I_{\text{th}}$ due to the FCA loss and it monotonically decreases with the increase of P_{input}. These results indicate that FCA induced by TPA is significant even at low excitation powers ($I_{\text{th}} = 120$ nW). This is possible because Q_S is very high in sample A and enhances nonlinear effects, and therefore the FCA influence rapidly grows above I_{th} with the start of lasing. It is interesting that the magnitude of the Q_S drop is not large enough to stop the lasing operation, probably due to the short carrier lifetime of approximately 1 ns. This is an advantage of the nanocavity device, which enables a large ratio of surface area to volume compared to cavities based on rib waveguides.

From the experimental results shown in Figs. 2(a)–2(c) and 3, we can conclude that the high Q_S is important for Raman Si lasers to reduce the threshold, but on the other hand the high Q_S implies a delayed rise of the Stokes signal and significant influence of the FCA at higher excitation powers. Therefore, the appropriate magnitude of Q_S has to be determined for each application. The delay of the Stokes signal's rise and the nanosecond lifetime after the pump pulse end are features of Raman Si lasers using high-Q cavities. Thus, it will be difficult to directly utilize the Raman Si nanocavity lasers for the duplication of short pulse signals with approximately100 Mbps or for the generation of ultrashort pulses.

For future device design it is important to estimate the free-carrier density at the threshold intensity I_{th}. The additional loss factor due to the FCA (Q_{FCA}) for excitation with I_{th} is estimated from the following relation:

$$\frac{1}{Q_{\text{FCA}}} = \frac{1}{Q_{\text{th}}} - \frac{1}{Q_S}. \tag{1}$$

Here, Q_{th} is the Q_S factor at the threshold intensity, i.e., 1.66×10^6, and Q_S is the intrinsic value (2.35×10^6). With these values we obtain a Q_{FCA} of 5.65×10^6. The absorption coefficient that determines the strength of the FCA (α_{FCA}) can be evaluated using [36]

$$Q_{\text{FCA}} = \frac{2\pi n_0}{\alpha_{\text{FCA}} \lambda_S}, \tag{2}$$

where n_0 is the refractive index. This equation assumes that the light confined in the cavity travels with phase velocity and is absorbed according to the absorption coefficient. By substituting 5.65×10^6 for Q_{FCA}, we

obtain $\alpha_{\mathrm{FCA}} = 2.51 \times 10^{-2}$ cm^{-1}. Finally, we evaluate the free-carrier density (N_{FCA}) with the following relation:

$$\alpha_{\mathrm{FCA}} = N_{\mathrm{FCA}} \sigma_{\mathrm{FCA}}. \tag{3}$$

Here, the absorption cross section for FCA, σ_{FCA}, is 1.06×10^{-17} cm^2, according to a previous report [37]. Therefore, the free-carrier density N_{FCA} at the threshold intensity is estimated to be 2.36×10^{15} cm^{-3}. Adding a lateral *p-i-n* diode structure with reverse bias to the nanocavity-based Raman Si laser can be a promising method to decrease the N_{FCA} since it shortens the carrier lifetime [12–15]. However, the doping density required to form the *p-i-n* structure is larger than 10^{18} cm^{-3} and the doped area should be close to the nanocavity [38]. Therefore, we also have to consider the FCA loss originating from the dopants in the *p* and *n* regions in such devices [39]. An important alternative method to shorten the carrier lifetime in the nanocavity laser would be a decrease of N_{FCA} by modifying the surface condition or cavity structure.

V. TIME-DOMAIN MEASUREMENTS IN THE HIGH EXCITATION REGIME

In this section, we present the time-resolved results obtained from sample B under strong excitation of the pump mode. Figures 4(a) and 4(b) show the time evolution of the emission from the pump mode and the Stokes mode, respectively, for four different excitation intensities ($P_{\mathrm{input}} = 1.3 \times I_{\mathrm{th}}$, $2.7 \times I_{\mathrm{th}}$, $5.3 \times I_{\mathrm{th}}$, and $8.0 \times I_{\mathrm{th}}$). The width of the pulsed light is 9 μs and the repetition rate is 83.3 kHz. The low signal-to-noise ratio in Fig. 4(a) is due to the neutral density filters that are inserted to reduce the emission power entering the photomultiplier. This procedure is necessary to ensure an accurate TCSPC measurement. Before we discuss the details of the transient responses in Figs. 4(a) and 4(b), we note that in these measurements λ_{in} is fixed at $\lambda_p + 3.6$ pm in order to include the shift of the resonant wavelength under high powers, which is explained in the following.

Figure 4(c) shows the resonant emission spectra of the pump mode for $P_{\mathrm{input}} = 1.0 \times I_{\mathrm{th}}$ (solid line) and $P_{\mathrm{input}} = 0.07 \times I_{\mathrm{th}}$ (dashed line) obtained in the cw measurements. The resonant peak for $1.0 \times I_{\mathrm{th}}$ exhibits a redshift of 3.6 pm compared to the λ_p obtained for $0.07 \times I_{\mathrm{th}}$. The redshift can be explained with the change of the refractive index via the carrier-plasma effect and the thermo-optic effect induced by TPA carriers [26]. The plasma effect lowers the refractive index, which is immediately reflected in the carrier generation rate. On the other hand, the thermal effect gradually increases the refractive index. For $P_{\mathrm{input}} > I_{\mathrm{th}}$, the influence of the thermal effect is larger than that of the plasma effect and thus the resonant peak shows a redshift. Therefore, the power coupled into the

cavity gradually increases during intense pulsed excitation (where effective redshift due to heating occurs as explained in the next paragraph) when λ_{in} is set to a longer wavelength than λ_p. As a result, P_{output} also becomes larger.

In the following we discuss the time-resolved responses in Figs. 4(a) and 4(b). The pump emission for $1.3 \times I_{\mathrm{th}}$ in Fig. 4(a) gradually increases within a time of more than 1000 ns, which suggests that the resonant peak of the pump mode gradually redshifts toward λ_{in} due to the increase of the cavity temperature. On the other hand, the corresponding Stokes signal in Fig. 4(b) starts to rise at 600 ns, which indicates that the photon density in the pump mode exceeds the threshold density at 600 ns. It is important to note that the rise behaviors of the pump and the Stokes emissions are different from those shown in Figs. 3(a) and 3(b). This difference is assigned to the change of λ_{in}. Furthermore, the Stokes signal for $1.3 \times I_{\mathrm{th}}$ in Fig. 4(b) shows a maximum intensity at about 1300 ns, which indicates that the resonant peak of the pump mode matches λ_{in} at 1300 ns. After 1300 ns, the intensity gradually decreases and converges to a stable level. This slow drift suggests that the redshift of the resonant peak of the pump mode proceeds due to further heating until thermal equilibrium is reached about 1 μs later. As explained above, the continued redshift across the optimum value, that is λ_{in}, results in a decrease of the photon density and the Stokes signal. The decrease of the Stokes emission after 1300 ns is more evident compared to that of the pump emission because of the nonlinear response of SRS to the pump photon density [see Eqs. (4) and (5)].

The Stokes signal for $P_{\mathrm{input}} = 2.7 \times I_{\mathrm{th}}$ shows a faster response time for the initial rise and a larger reduction after the initial rise compared to the data for $1.3 \times I_{\mathrm{th}}$, because the higher excitation power increases the magnitude of the resonance peak shift. A very interesting trend is observed for $P_{\mathrm{input}} = 5.3 \times I_{\mathrm{th}}$. As expected, the response time is faster and the reduction after the initial rise is more drastic, but then a peculiar oscillating behavior is observed, which slowly loses its amplitude until thermal equilibrium is reached. These oscillations are explained with alternating redshifts and blueshifts of the resonant peak induced by thermal and plasma effects. Such a behavior is possible for a strong excitation, which creates a large nonequilibrium (the detailed mechanism is explained in Sec. VI). The peak shifts of the pump nanocavity mode are always accompanied by a change of the photon density in the cavity, which results in large variations of both pump and Stokes signals. Therefore, the oscillations can be observed in both Figs. 4(a) and 4(b). We find that the oscillations completely disappear about 1 μs after the initial rise and the intensity reaches a stable level.

We emphasize that this oscillating behavior is not related to the relaxation oscillations observed for usual semiconductor lasers with a picosecond response time [40]. Further investigation of the picosecond responses of
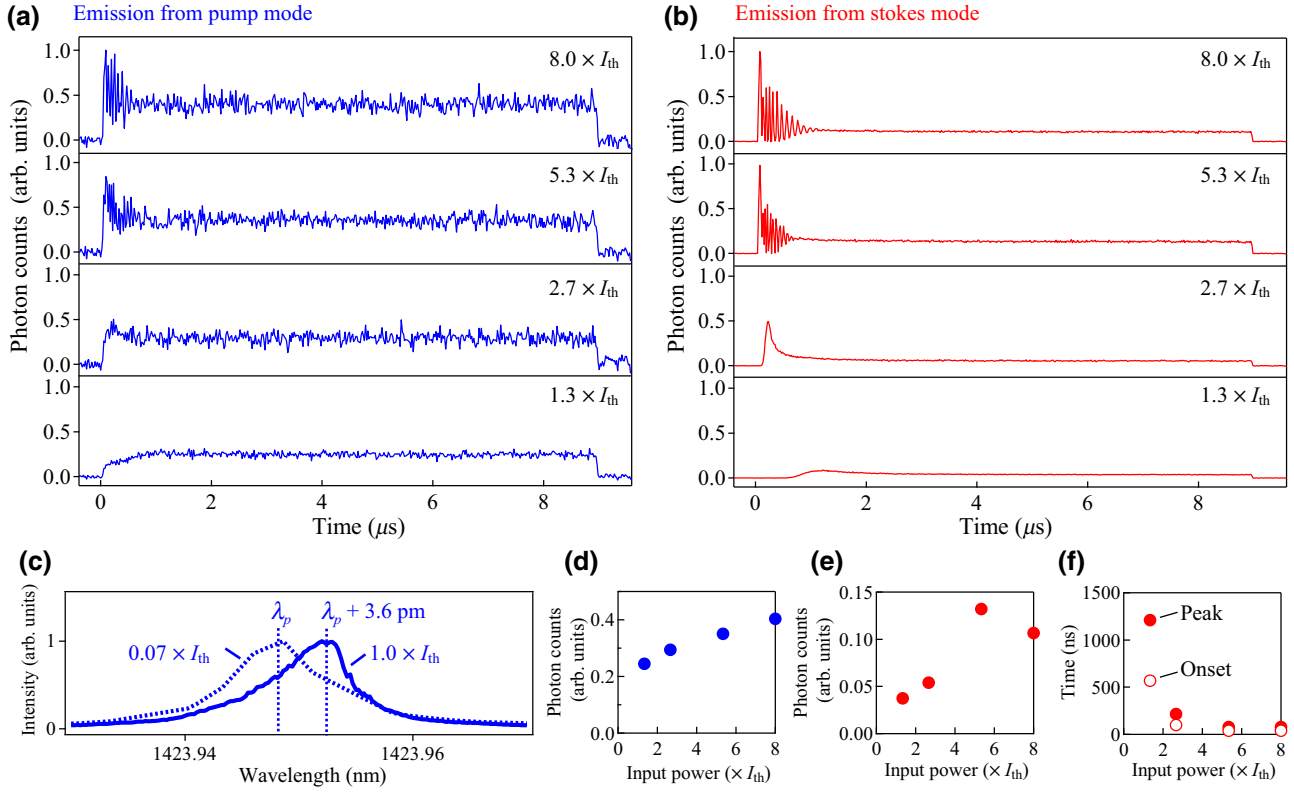
FIG. 4. (a) Time-resolved emission intensities from the pump mode and (b) the Stokes mode for various P_{input}. The excitation wavelength is set to $\lambda_p + 3.6$ pm. (c) Resonant spectra of the pump mode for $P_{\text{input}} = 1.0 \times I_{\text{th}}$ (solid line) and $P_{\text{input}} = 0.07 \times I_{\text{th}}$ (dashed line). (d) Averaged intensities of the pump emission data in (a) between 6.0 and 9.0 μs. (e) Averaged intensities of the Stokes emission data shown in (b). (f) Power dependence of the response times for the initial peak of the Stokes signal shown in (b). Open circles represent the onset delay. Filled circles show the temporal position of the peak maximum.

Raman Si nanocavity lasers may be interesting, since a phenomenon similar to the relaxation oscillation could be found [41]. We note that the resonant wavelength shift of the Stokes nanocavity mode is not the primary cause for the oscillation in this experiment, because the magnitude of the shift (approximately 10 pm) is much smaller than the Raman gain width (approximately 630 pm) [42]. We observe such an oscillation behavior of the pump emission even for high-Q nanocavities without Raman lasing. Similar oscillating behaviors have been also reported in emissions from microring and microdisk cavities [43,44]. The critical slowing down and overshooting in bistable systems are well-known phenomena that are related to these oscillations [41,45]. It is noted that Fig. 4(b) is the first observation of oscillations in the Raman nanocavity laser emission.

The Stokes data for the highest excitation in Fig. 4(b) ($8.0 \times I_{\text{th}}$) reveal that the amplitude and the duration (> 1 μs) of the oscillations in the Stokes signal increase upon stronger excitation. It is interesting that the peak intensity of the initial peak is the same as that for $5.3 \times I_{\text{th}}$, which suggests that the optical loss due to FCA can be comparable to the Raman gain when the resonant peak of

the pump mode matches λ_{in}. In other words, the net gain is saturated for this excitation intensity. This observation agrees with the P_{input}-P_{output} relation shown in Fig. 2(f). Therefore, no improvement of the output power can be expected for higher values of P_{input}.

Figures 4(d) and 4(e) show the input power dependence of the averaged intensities for the pump and Stokes mode emissions shown in Figs. 4(a) and 4(b), respectively. The averaging is performed over the stable time range extending from 6.0 to 9.0 μs. The pump intensity in Fig. 4(d) increases monotonically while the Stokes intensity in Fig. 4(e) has its maximum at $P_{\text{input}} = 5.3 \times I_{\text{th}}$. The drop observed for $P_{\text{input}} = 8.0 \times I_{\text{th}}$ can be suppressed to some extent by optimizing λ_{in} as shown in Fig. 5, which will be explained later. Figure 4(f) summarizes the onset delay and the temporal position of the first peak in the Stokes signal. It is evident that the responses of the initial lasing signal become drastically faster for higher excitation powers. The response times also depend on λ_{in} as demonstrated later in Fig. 5.

The above discussion clarified that the power-dependent dynamic shift of the resonant peak has various consequences for the Raman laser dynamics. We consider that
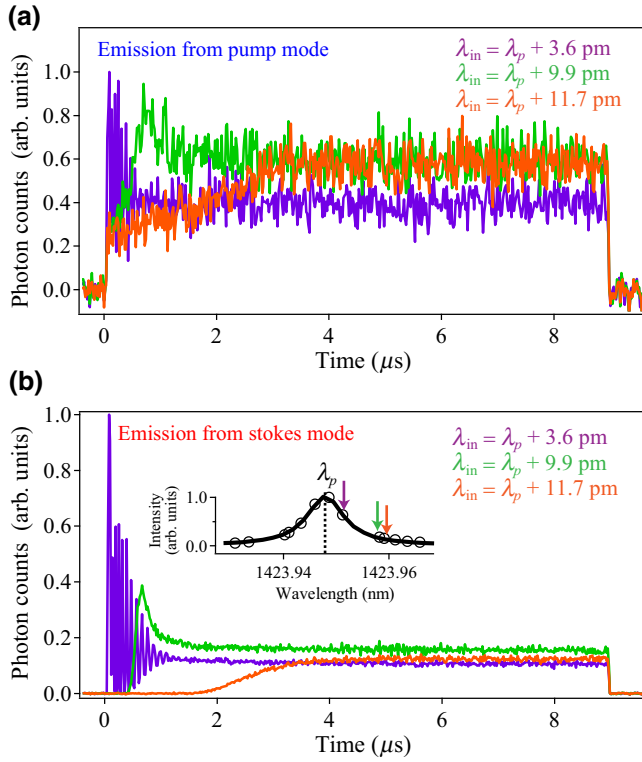
FIG. 5.   (a) Time-resolved emission intensities from the pump mode and (b) the Stokes mode of sample B for various excitation wavelengths. The excitation power is $8 \times I_{\text{th}}$. The inset shows the relation between the excitation wavelengths and the intrinsic resonant emission spectrum of the pump mode.

the dynamic shift is one of the major reasons for a reduced Raman laser output, because the peak intensity that is observed when the resonant peak matches λ_{in} during the initial rise is larger than the intensity observed for the equilibrium state at late times, as shown in Fig. 4(b). We consider that this explanation can be also applied to other types of Raman Si lasers using high-Q cavities.

To confirm the above conclusions, we investigate the influence of λ_{in} on P_{output} for $P_{\text{input}} = 8.0 \times I_{\text{th}}$. We mainly focus on the discussion of the Stokes signal. The λ_{in} dependence of the pump signal is similar to that of the Stokes signal. Figures 5(a) and 5(b) show the time-resolved signals of the pump and Stokes emission, respectively. The purple lines represent the signals for $\lambda_{\text{in}} = \lambda_{\text{p}} + 3.6$ pm, the green lines correspond to $\lambda_{\text{in}} = \lambda_p + 9.9$ pm, and the orange lines are for $\lambda_{\text{in}} = \lambda_p + 11.7$ pm. The inset in Fig. 5(b) shows the relation between the intrinsic resonant emission spectrum of the pump mode and the three excitation wavelengths. The purple data are the same as the data for the highest excitation shown in Figs. 4(a) and 4(b).

When λ_{in} is set to $\lambda_p + 9.9$ pm, the Stokes signal [Fig. 5(b); green curve] starts to rise at 400 ns and shows a maximum at 660 ns. Then it decreases and converges to

a stable emission level, which is reached at approximately 2 μs. These characteristic response times are delayed compared to those for $\lambda_p + 3.6$ pm [Fig. 5(b); purple data]. In addition, an oscillation is not observed because the detuning between λ_p and λ_{in} is too large to create a strong nonequilibrium, which will be discussed in Sec. VI. The Stokes intensity under thermal equilibrium is 1.5 times larger than that observed for excitation with $\lambda_p + 3.6$ pm, which suggests that the resonant peak of the pump mode in the thermal equilibrium is closer to $\lambda_p + 9.9$ pm.

When λ_{in} is set to $\lambda_p + 11.7$ pm, the Stokes signal begins to rise at 1500 ns. It gradually becomes stronger as the temperature increases and converges to a stable intensity at approximately 4 μs. It is interesting that the signal exhibits no reduction after the initial rise, which indicates that the resonant peak of the pump mode stayed below λ_{in}. Consequently, an oscillation is not observed. The intensity at the equilibrium condition is smaller than that observed for excitation at $\lambda_p + 9.9$ pm but larger than that at $\lambda_p + 3.6$ pm. We confirm that for this P_{input} no Raman lasing is observed for excitation wavelengths above $\lambda_p + 11.7$ pm.

Figure 5 demonstrates that the initial lasing behavior strongly depends on λ_{in}. It should be emphasized that the Raman laser converges to a stable cw operation for any excitation condition that is employed in our experiments. This feature will be important for the application as a cw laser source in photonic circuits. On the other hand, the instable regime may allow a self-pulsating operation of our Raman laser device, which is useful for certain applications [43]. In order to maximize P_{output}, we have to appropriately tune λ_{in} to take into account the dynamic shift. To reduce the response time of the Stokes signal shown in Fig. 4(f), which is useful for application in all-optical switching devices, λ_{in} should be tuned close to λ_p, because the pump photon density can exceed the threshold faster due to a higher coupling efficiency. However, the intensity drops after the initial rise due to the dynamic shift, which is enhanced in such a case. Practically, it can be difficult to tune λ_{in} close to λ_p and instead it may be more convenient to tune λ_p with an additional microheater near the cavity [35,46].

From the results of Figs. 3–5, we consider that P_{output} can be significantly enhanced if we reduce the TPA carriers by adding a lateral *p-i-n* diode, increasing the operation wavelength to mid-infrared or utilizing other materials with higher band-gap energies [47]. This will decrease the loss through FCA as well as the intensity drop of P_{output} after the initial rise caused by the dynamic shift. Furthermore, the oscillating behavior will also be reduced, which is important for the practical application of the Raman laser. We consider that use of a superluminescent diode for the excitation may solve the problem of the dynamic wavelength shift because of its broad emission spectrum.

VI. THEORETICAL INVESTIGATION OF THE LASING OSCILLATIONS

In this section, we numerically investigate the mechanism of the lasing oscillations observed in Fig. 4(b) by employing a calculation framework that is based on coupled mode theory (CMT) [48,49].

The time evolution of the number of photons confined in the two nanocavity modes can be calculated with the differential equation for the amplitude of the pump light (a_p) [48],

$$\frac{da_p}{dt} = \left(-\frac{1}{2\tau_{p,\text{total}}} + i\omega'_p\right)a_p - g_R^{\text{cav}}(N_S + 1)a_p + \sqrt{\frac{P_{\text{in}}}{2\tau_{p,\text{in}}}}e^{i\omega_{\text{in}}t}, \qquad (4)$$

and that for the number of photons in the Stokes mode (N_S) [49],

$$\frac{dN_S}{dt} = -\frac{N_S}{\tau_{S,\text{total}}} + 2g_{R,\text{detuning}}^{\text{cav}}(N_S + 1)N_p. \qquad (5)$$

The amplitude and the photon number are related via $N_i = |a_i|^2/\hbar\omega_i$ where the index i can be replaced with either p or S for the pump or Stokes mode, respectively. It is noted that the pump mode needs to be represented with an amplitude because the pump mode is coherently excited by a monochromatic light. $\tau_{i,\text{total}}$ is the photon lifetime of the cavity mode, which includes both the photon leakage from the cavity and the losses due to TPA [see Appendix, Eq. (A1)]. ω'_p is the angular frequency of the resonant peak for the pump mode that shifts according to the refractive index determined by the carrier-plasma effect, the thermo-optic effect, and the Kerr effect [see Appendix Eq. (A8)]. These effects, which are induced by TPA carriers, are also taken into account for the resonance frequency of the Stokes mode, ω'_s, although we obtained almost the same results without the dynamic shift of ω'_s. The Raman gain coefficient of the nanocavity is g_R^{cav} [see Appendix Eq. (A14)] and $g_{R,\text{detuning}}^{\text{cav}}$ is the Raman gain coefficient considering the detuning between the peak of the spontaneous Raman scattering and the resonant peak of the Stokes mode [see Appendix Eq. (A16)]. Accordingly, the terms $g_R^{\text{cav}}N_S a_p$ and $g_R^{\text{cav}}a_p$ in Eq. (4) describe the SRS and spontaneous Raman scattering, respectively. The terms $2g_{R,\text{detuning}}^{\text{cav}}N_S N_p$ and $2g_{R,\text{detuning}}^{\text{cav}}N_p$ in Eq. (5) represent the same mechanisms, since a_p and N_p are interchangeable. The last term in Eq. (4), $\sqrt{P_{\text{in}}/2\tau_{p,\text{in}}}e^{i\omega_{\text{in}}t}$, represents the excitation light that is coupled into the pump mode. Here, $1/\tau_{p,\text{in}}$ is the coupling strength between the propagating light in the pump excitation waveguide and the pump nanocavity mode, P_{in} is the input power of the excitation light in the pump waveguide, and $\omega_{\text{in}} = 2\pi c/\lambda_{\text{in}}$.

The temporal evolution of the free-carrier density in the nanocavity, N, is expressed with

$$\frac{dN}{dt} = -\frac{N}{\tau_{\text{carrier}}} + G_{\text{carrier}}, \qquad (6)$$

where τ_{carrier} is the dissipation time of the free carriers in the nanocavity, determined by nonradiative recombination and carrier diffusion. G_{carrier} is the generation rate of free carriers, i.e., the free carriers generated by the TPA process [the equation that governs these processes is given in the Appendix Eq. (A17)]. The energy of the light absorbed by TPA and FCA is finally converted into heat through three processes [Appendix Eqs. (A18)–(A21)] and induces a temperature rise of the cavity material. Here, the heating effect due to phonons generated by SRS is not considered because this effect should be minor.

In order to properly evaluate the temperature change of the nanocavity, we considered the cavity and the PC surrounding the cavity. The heat generated in the cavity diffuses to the surrounding PC. The changes in cavity temperature and surrounding temperature are described as ΔT_{cav} and $\Delta T_{\text{surround}}$, respectively. They are evaluated by

$$\frac{d\Delta T_{\text{cav}}}{dt} = -\frac{\Delta T_{\text{cav}} - \Delta T_{\text{surround}}}{\tau_{\text{thermal, cav}}} + G_{\text{thermal}}, \qquad (7)$$

and

$$\frac{d\Delta T_{\text{surround}}}{dt} = -\frac{\Delta T_{\text{surround}}}{\tau_{\text{thermal,surround}}} + \frac{C_v^{\text{cav}}}{C_v^{\text{surround}}}\frac{\Delta T_{\text{cav}} - \Delta T_{\text{surround}}}{\tau_{\text{thermal,cav}}}, \qquad (8)$$

where G_{thermal} [see Appendix Eq. (A18)] and $1/\tau_{\text{thermal}}$ are the heat generation rate and the temperature decay rate, respectively. Equation (8) shows that the surrounding PC is responsible for allowing a thermal equilibrium with the thermal reservoir (environment) according to the time constant $\tau_{\text{thermal,surround}}$. The heat capacities of the cavity and the surrounding PC are C_v^{cav} and C_v^{surround}, respectively.

Figure 6 shows the calculation results for an excitation power of $11 \times I_{\text{th}}$ and an excitation wavelength of $\lambda_{\text{in}} = \lambda_p + 3.6$ pm. These conditions are almost the same as those for Fig. 4. The initial process is divided into four time domains, (i)–(iv), shown with different colors. The detailed parameters are summarized in Table II in the Appendix.

The blue and red curves in Fig. 6(a) show the normalized time evolution of the number of photons in the pump mode, $N_p = |a_p|^2/\hbar\omega_p$, and the Stokes mode, N_S, respectively. The curves are normalized with the corresponding peak values at 124 ns. Both signals oscillate, and the oscillation amplitude of the Stokes mode is larger than that for the pump mode. Although the calculation results have a longer response time for the initial rise when compared
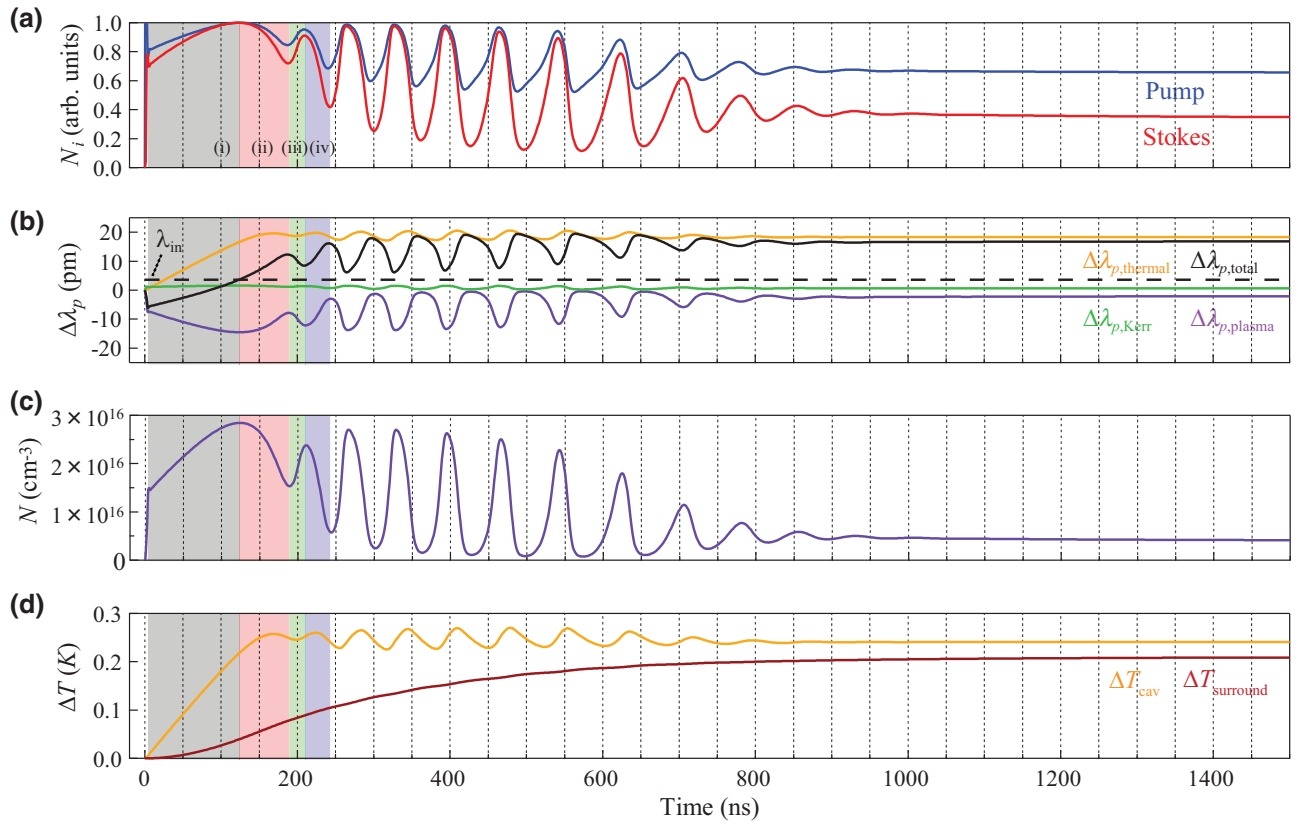
FIG. 6.   (a) Calculated normalized time evolution of the number of photons in the pump mode and the Stokes mode. (b) Total shift of the resonance peak wavelength for the Stokes mode, as well as the individual contributions due to carrier-plasma effect, thermo-optic effect, and Kerr effect. (c) Carrier density generated by TPA. (d) Temperature of the cavity and the surrounding PC.

with the experimental results, the oscillation period almost agrees with that measured in the experiment. The calculation predicts that the amplitude of the oscillation gradually decreases and that the emission converges to a stable level within 1 μs after the initial rise, in agreement with the experiment shown in Figs. 4(a) and 4(b).

Figure 6(b) shows the shift of the resonant wavelength ($\Delta\lambda_p$) for the pump nanocavity mode. The total shift ($\Delta\lambda_{p,\text{total}}$) from the intrinsic value λ_p and the individual contributions from the carrier-plasma effect ($\Delta\lambda_{p,\text{plasma}}$), the thermo-optic effect ($\Delta\lambda_{p,\text{thermal}}$), and the Kerr effect ($\Delta\lambda_{p,\text{Kerr}}$) are shown in black, purple, orange, and green, respectively. The dashed horizontal line represents the position of λ_{in}. At 124 ns, $\Delta\lambda_{p,\text{total}}$ reaches the value of λ_{in}. It is important to note that the magnitude of the oscillation for $\Delta\lambda_{p,\text{plasma}}$ is the largest among the three contributions and thus the oscillation of $\Delta\lambda_{p,\text{total}}$ is almost synchronous with that for $\Delta\lambda_{p,\text{plasma}}$ except for the time domains (i) and (ii). It is apparent that the Kerr effect is much smaller. Therefore, we omit the Kerr effect in the explanation of the experimental part and the following discussion. We confirm that the resonant peak shift of the Stokes nanocavity mode behaves similarly.

Figure 6(c) shows the TPA carrier density, N, which is generated by TPA. Note that the oscillation of the carrier density and the oscillation of N_i [Fig. 6(a)] have the same phase while the oscillation of the carrier density and the oscillation of $\Delta\lambda_{p,\text{plasma}}$ [Fig. 6(b); purple data] have opposite phases. Figure 6(d) presents the temperature changes of the cavity and the surrounding PC. The oscillations of the cavity temperature and $\Delta\lambda_{p,\text{thermal}}$ [Fig. 6(b); orange data] have the same phase. The oscillation amplitude of the cavity temperature is relatively small, and is obviously not in phase with N_i, $\Delta\lambda_{p,\text{total}}$, and N. This unsymmetrical behavior, which originates from the difference between the response time of the carrier-plasma effect and that of the thermo-optic effect, is the reason for the oscillations of the pump and Stokes mode emissions, as explained below.

The calculation results enable a detailed explanation of the oscillation mechanism. First, we discuss the time domain (i). Here, the blueshift of the resonant peak of the pump mode occurs simultaneously with the excitation due to the plasma effect as shown in Fig. 6(b). Then the resonant peak redshifts due to the increase of the cavity temperature. It is noted that the magnitude of the redshift is reduced by the increase of the plasma effect in this

TABLE II.   Parameters used for the calculations.

Parameter	Symbol	Value	Source
Wavelength of pump mode	λ_p	1423.9480	Experiment
Wavelength of Stokes mode	λ_S	1538.0479	Experiment
Frequency spacing between the pump mode (f_p) and the Stokes mode (f_S)	Δf	15.614 THz	Experiment
Pump mode total Q	Q_p	1.66×10^5	Experiment
Pump mode in-plane Q	$Q_{p,\text{in}}$	1.03×10^6	Experiment
Pump mode vertical Q	$Q_{p,v}$	1.98×10^5	Experiment
Stokes mode total Q	Q_S	1.59×10^6	Experiment
Stokes mode in-plane Q	$Q_{S,\text{in}}$	2.90×10^6	Experiment
Stokes mode vertical Q	$Q_{S,v}$	3.52×10^6	Experiment
Free-carrier lifetime	τ_{carrier}	1.4 ns	Experiment
Cavity temperature lifetime	$\tau_{\text{thermal,cav}}$	60 ns	Experiment
Cavity surrounding PC temperature lifetime	$\tau_{\text{thermal,surround}}$	2000 ns	Experiment
Heat capacity ratio between cavity and surrounding PC	$C_v^{\text{cav}}/C_v^{\text{surround}}$	0.2	Experiment
TPA mode volume of pump mode	$V_{p,\text{TPA}}$	0.35×10^{-18} m^3	FDTD
TPA mode volume of Stokes mode	$V_{S,\text{TPA}}$	0.33×10^{-18} m^3	FDTD
TPA overlap mode volume between pump mode and Stokes mode	$V_{o,\text{TPA}}$	0.71×10^{-18} m^3	FDTD
Volume of cavity	V_{cav}	0.40×10^{-18} m^3	$\sim$L $\times$ W $\times$ H
Refractive index of silicon	$n_{p\,(S)}$	3.46	[51]
TPA coefficient	β_{Si}	4.4×10^{-12} m/W	[4]
Relaxation time	τ_{relax}	0.17 ps for electrons	[51]
		0.10 ps for holes	
Effective mass	$m*$	0.30 m_0 for electrons	[51]
		0.45 m_0 for holes	
		m_0: electron rest mass	
Temperature dependence of refractive index	dn_i/dT	1.85×10^{-4} K^{-1}	[52]
Kerr coefficient	n_2	4.4×10^{-18} m^2/W	[53]
Bulk Raman gain coefficient	g_R^B	2.9×10^{-10} m/W	[5]
Raman mode volume	V_R	0.48×10^{-18} m^3	FDTD
Raman shift of Si	Δf_R	15.606 THz	[30]
Raman gain width	Δ	0.08 THz	[42]

domain, because the resonant peak is shorter than λ_{in}. In time domain (ii), after the peak wavelength becomes larger than λ_{in} at 124 ns, the carrier density decreases as shown in Fig. 6(c) because the photon density in the cavity decreases as shown in Fig. 6(a). The reduction of the carrier density decreases the plasma effect and therefore the redshift of the resonant peak accelerates. On the other hand, the reduction of the carrier density stops the increase of the cavity temperature and after a short delay the cavity begins to cool, which suppresses the reduction of the plasma effect and thus inhibits any further redshift. As a result, the resonant peak redshifts to a wavelength that is 8.7 pm longer than λ_{in}. Then, in time domain (iii), $\Delta\lambda_{p,\text{total}}$ starts to blueshift at 190 ns, driven by the cooling. This is accompanied by an increase of the plasma effect because the photon density and carrier density start to increase as $\Delta\lambda_{p,\text{total}}$ approaches λ_{in}. Consequently, the blueshift is accelerated. On the other hand, the increase of the carrier density stops the cooling of the cavity temperature with a slight delay due to the heat generation and the cavity starts to heat up again. Finally, in time domain (iv), the redshift of $\Delta\lambda_{p,\text{total}}$ occurs again before the resonant peak matches λ_{in}. By repeating these

cycles of redshift and blueshift, the gap between ΔT_{cav} and $\Delta T_{\text{surround}}$ is decreasing and the nanocavity converges to the thermal equilibrium condition. Finally, the oscillation disappears.

From these calculations, it is concluded that the key condition for the existence of the oscillation is whether the resonant peak can redshift to a wavelength much longer than λ_{in} during the first redshift in time domains (i) and (ii) or not. For this phenomenon, the large acceleration of the redshift due to the decrease of the plasma effect is important, which appears at the beginning of time domain (ii). If the detuning between λ_p and λ_{in} is large, the oscillation becomes weak or does not appear. Therefore, an oscillation is not observed in Fig. 5 for large detunings of 9.9 and 11.7 pm. It should be noted that such an oscillation may occur even without the thermo-optic effect if the cavity and the pump parameters are chosen differently [41].

VII. CONCLUSIONS

The time-domain measurements for nanocavity-based Raman Si lasers reveal that TPA carriers induce various

dynamic effects in the lasing process. The loss through FCA as a result of efficient TPA is observed even for the threshold excitation intensity, i.e., 0.12 μW, where we estimate a free-carrier density of 2.36×10^{15} cm^{-3}. The TPA carriers cause a dynamic shift of the resonant wavelength of the pump nanocavity mode via the thermo-optic effect and the carrier-plasma effect. This dynamic shift causes a reduction of the Raman laser output after the initial rise and furthermore it can induce oscillations under certain conditions, which are clarified theoretically. We find that the optical responses strongly depend on the excitation wavelength and the excitation power. An important point is that the Raman laser converges to a stable cw operation within a few microseconds after the initial rise for all excitation conditions. These results will be useful to design suitable device structures that employ the advantages of the Raman silicon nanocavity lasers.

APPENDIX

CMT Calculation and Parameters

Here we present the details of the equations in Sec. VI.
$1/\tau_{i,\text{total}}$ (i = p, S) is the rate of the energy loss in the cavity. It has several contributions,

$$1/\tau_{i,\text{total}} = 1/\tau_{i,\text{in}} + 1/\tau_{i,v} + 1/\tau_{i,\text{TPA}} + 1/\tau_{i,\text{FCA}}, \quad (A1)$$

where $1/\tau_{i,\text{in}}$ and $1/\tau_{i,v}$ are the rates of energy transfer into the waveguide (in-plane direction) and into free space (vertical direction), respectively, and are calculated via $1/\tau_{i,\text{in(v)}} = \omega_i/Q_{i,\text{in(v)}}$. In the coupled mode theory, $Q_{i,v}$ can be expressed as follows [50]:

$$Q_{i,v} = Q_i/\sqrt{T_i}. \quad (A2)$$

Here, T_i is the transmittance at λ_i, which are 0.7 and 0.3 for the pump mode and Stokes mode, respectively. $Q_{i,\text{in}}$ is determined from the relationship $1/Q_i = 1/Q_{i,\text{in}} + 1/Q_{i,v}$ at a low-power excitation condition. These Q factors are summarized in Table II.

The third term on the right-hand side of Eq. (A1), $1/\tau_{i,\text{TPA}}$, is the loss rate due to TPA and is proportional to

the energy stored in the cavity. According to Ref. [48] the loss rates in the pump and Stokes modes can be written as

$$\frac{1}{\tau_{p,\text{TPA}}} = \frac{\beta_{\text{Si}}c^2}{n_p^2 V_{p,\text{TPA}}}|a_p|^2 + \frac{\beta_{\text{Si}}c^2}{n_p^2 V_{o,\text{TPA}}}2|a_S|^2, \quad (A3)$$

and

$$\frac{1}{\tau_{S,\text{TPA}}} = \frac{\beta_{\text{Si}}c^2}{n_S^2 V_{S,\text{TPA}}}|a_S|^2 + \frac{\beta_{\text{Si}}c^2}{n_S^2 V_{o,\text{TPA}}}2|a_p|^2, \quad (A4)$$

where the first terms represent the TPA due to two pump photons or two Stokes photons. The second terms represent the process where one pump photon and one Stokes photon are absorbed simultaneously. β_{Si} is the TPA coefficient of bulk silicon. The effective mode volume for TPA, $V_{i,\text{TPA}}$, is [48]

$$V_{i,\text{TPA}} = \frac{\left(\int n_i^2(r)|E_i(r)|^2 dr^3\right)^2}{\int_{\text{Si}} n_i^4(r)|E_i(r)|^4 dr^3}. \quad (A5)$$

$V_{o,\text{TPA}}$ indicates the spatial overlap between the pump mode and the Stokes mode, and we consider $V_{o,\text{TPA}} = V_R$, which is provided in Eq. (A15).

The last term in Eq. (A1), $1/\tau_{i,\text{FCA}}$, is the loss rate due to FCA and is proportional to the time-dependent carrier density, given with

$$\frac{1}{\tau_{i,\text{FCA}}} = \frac{c}{n_i}(\sigma_{i,e} + \sigma_{i,h})N(t). \quad (A6)$$

c is the velocity of light in vacuum. The absorption cross sections for electrons and holes $\sigma_{i,e/h}$, can be written as

$$\sigma_{i,e/h} = \frac{e^2}{cn_i\omega_i^2\varepsilon_0 m_{e/h}^*\tau_{\text{relax},e/h}}, \quad (A7)$$

where e is the electron charge, ϵ_0 is the dielectric constant in vacuum, m_e^* and m_h^* are the effective masses of electrons and holes, respectively, and $\tau_{\text{relax},e/h}$ is the corresponding relaxation time.

ω_i' (i = p, S) is the shifted resonance frequency for the pump mode or the Stokes mode. The shift occurs via three nonlinear effects: the carrier-plasma effect, the thermo-optic effect, and the Kerr effect, which can be written as

$$\omega_i'(t) = \omega_i - \frac{\Delta n_{i,\text{carrier}}}{n_i}\omega_i - \frac{\Delta n_{i,\text{thermal}}}{n_i}\omega_i - \frac{\Delta n_{i,\text{Kerr}}}{n_i}\omega_i. \quad (A8)$$

The refractive index of Si for the pump mode and Stokes mode is given with n_i (i = p, S), and $\Delta n_{i,\text{carrier}}$, $\Delta n_{i,\text{thermo}}$, and $\Delta n_{i,\text{Kerr}}$ are the individual shifts of the refractive index due to the carrier-plasma effect, the thermo-optic effect,

and the Kerr effect, respectively. The individual shifts are defined with [48]

$$\Delta n_{p,\text{carrier}} = \frac{e^2 N}{2\varepsilon_0 n_p \omega_{\text{in}}^2} \left(\frac{1}{m_e^*} + \frac{1}{m_h^*} \right), \quad \text{(A9)}$$

$$\Delta n_{S,\text{carrier}} = \frac{e^2 N}{2\varepsilon_0 n_S \omega_S^2} \left(\frac{1}{m_e^*} + \frac{1}{m_h^*} \right), \quad \text{(A10)}$$

$$\Delta n_{i,\text{thermal}} = \frac{dn_i}{dt} \Delta T, \quad \text{(A11)}$$

$$\Delta n_{p,\text{Kerr}} = \frac{cn_2}{n_p^2 V_{p,\text{Kerr}}} |a_p|^2 + \frac{cn_2}{n_p^2 V_{o,\text{Kerr}}} 2|a_S|^2, \quad \text{(A12)}$$

$$\Delta n_{S,\text{Kerr}} = \frac{cn_2}{n_S^2 V_{S,\text{Kerr}}} |a_S|^2 + \frac{cn_2}{n_S^2 V_{o,\text{Kerr}}} 2|a_p|^2. \quad \text{(A13)}$$

In Eq. (A11), we introduce the temperature dependence of the refractive index with dn_i/dt. In Eqs. (A12) and (A13), n_2 is the Kerr coefficient of bulk Si for propagating light and the effective modal volumes for the Kerr effect are $V_{i,\text{Kerr}} = V_{i,\text{TPA}}$ and $V_{o,\text{Kerr}} = V_{o,\text{TPA}}$.

g_R^{cav} is the Raman gain coefficient of the nanocavity and is defined as [49]

$$g_R^{\text{cav}} = \left(\frac{\hbar \omega_{\text{in}} c^2}{2 n_p n_S V_R} \right) g_R^{\text{bulk}}, \quad \text{(A14)}$$

where n_p and n_S are the refractive indices for the pump mode and Stokes mode, respectively. g_R^{bulk} is the Raman gain coefficient of bulk Si. V_R is the effective modal volume for Raman scattering, which determines the spatial overlap between the pump mode and the Stokes mode,

$$V_R = \frac{\int \varepsilon_p E_p^2 dV \int \varepsilon_S E_S^2 dV}{\varepsilon_p \varepsilon_S \sum_{ijkl} \int_{\text{Si}} \chi_{ijkl}^R E_{p,i} E_{S,j}^* E_{S,k} E_{p,l}^* dV}. \quad \text{(A15)}$$

Here, ε_i ($i = p, S$) is the dielectric constant in Si and E_i ($i = p, S$) is the electric field of the pump mode or the Stokes mode. χ_{ijkl}^R is the fourth-order tensor corresponding to the Raman effect in Si. It has to be noted that V_R depends on the crystal orientation and the overlap between the electric fields of the pump mode and the Stokes mode. By choosing the optimal crystal direction [100] for the nanocavity-based Raman Si laser, we are able to realize lasing operation [16]. $g_{R,\text{detuning}}^{\text{cav}}$ is the Raman gain coefficient that considers the detuning between the peak of the spontaneous Raman scattering and the resonant peak of the Stokes mode,

$$g_{R,\text{detuning}}^{\text{cav}} = g_R^{\text{cav}} \frac{((\Delta/2))^2}{(\omega'_S + \Delta f_R - \omega_{\text{in}})^2 + (\Delta/2)^2}, \quad \text{(A16)}$$

where Δ is the full width at half-maximum of the spontaneous Raman scattering in Si and Δf_R is the Raman shift of the Si nanocavity.

Finally, we specify the generation rates introduced in Eqs. (6) and (7). The generation rate of the free carriers G_{carrier} can be calculated from the mode-averaged TPA loss rate [48],

$$G_{\text{carrier}} = \frac{\beta_{\text{Si}} c^2}{2\hbar \omega_{\text{in}} n_p^2 V_{p,\text{FCA}}^2} |a_p|^4 + \frac{\beta_{\text{Si}} c^2}{2\hbar \omega'_S n_S^2 V_{S,\text{FCA}}^2} |a_S|^4$$
$$+ \frac{\beta_{\text{Si}} c^2}{\hbar(\omega_{\text{in}} + \omega'_S) n_p^2 V_{o,\text{FCA}}^2} 2|a_S|^2 |a_p|^2$$
$$+ \frac{\beta_{\text{Si}} c^2}{\hbar(\omega_{\text{in}} + \omega'_S) n_S^2 V_{o,\text{FCA}}^2} 2|a_p|^2 |a_S|^2. \quad \text{(A17)}$$

The effective mode volume for FCA is obtained from $V_{\text{FCA}}^2 = V_{\text{TPA}} \times V_{\text{carrier}}^{\text{cav}}$. The cavity volume for the free carriers is $V_{\text{carrier}}^{\text{cav}}$ and is defined as $V_{\text{carrier}}^{\text{cav}} = $ (cavity length)·(distance between the air holes nearest to the center of the cavity in the y direction)·(slab thickness) [26].

The heat generation rate G_{thermal} is given by

$$G_{\text{thermal}} = G_{\text{thermal,TPA-relax}} + G_{\text{thermal,FCA-relax}}$$
$$+ G_{\text{thermal,recomb}}. \quad \text{(A18)}$$

$G_{\text{thermal,TPA-relax}}$ is the heat generation rate due to relaxation of TPA carriers, $G_{\text{thermal,FCA-relax}}$ is the heat generation rate due to relaxation of carriers generated by FCA, and $G_{\text{thermal,recomb}}$ is the heat generation rate for nonradiative interband recombination of TPA carriers. We can calculate these terms as follows:

$$G_{\text{thermal,TPA-relax}} = \frac{|a_p|^2}{\tau_{p,\text{TPA}}} \times \frac{2\hbar \omega_{\text{in}} - E_g}{2\hbar \omega_{\text{in}}} \times \frac{1}{C_v^{\text{cav}}}$$
$$+ \frac{|a_S|^2}{\tau_{S,\text{TPA}}} \times \frac{2\hbar \omega_S - E_g}{2\hbar \omega_S} \times \frac{1}{C_v^{\text{cav}}} \quad \text{(A19)}$$

$$G_{\text{thermal,FCA-relax}} = \frac{|a_p|^2}{\tau_{p,\text{FCA}}} \times \frac{1}{C_v^{\text{cav}}} + \frac{|a_S|^2}{\tau_{S,\text{FCA}}} \times \frac{1}{C_v^{\text{cav}}} \quad \text{(A20)}$$

$$G_{\text{thermal,FCA-recomb}} = \frac{N V_{\text{carrier}}^{\text{cav}}}{\tau_{\text{carrier}}} \times E_g \times \frac{1}{C_v^{\text{cav}}} \quad \text{(A21)}$$

E_g is the band-gap energy of Si. For simplicity we assume that all carriers generated by TPA recombine in the surrounding PC region. In this calculation, the values of τ_{carrier}, $\tau_{\text{thermal,cav}}$, $\tau_{\text{thermal,surround}}$, and $C_v^{\text{cav}}/C_v^{\text{surround}}$ are fitted to match the experimental results.

────────

[1] L. Pavesi, S. Gaponenko, and L. Dal Negro, *Towards the First Silicon Laser* (Kluwer Academic, Dordrecht, 2003).

[2] S. S. Iyer and Y. H. Xie, Light emission from silicon, Science **260**, 40 (1993).

[3] R. Claps, D. Dimitropoulos, Y. Han, and B. Jalali, Observation of Raman emission in silicon waveguides at 1.54 μm, Opt. Express **10,** 1305 (2002).

[4] R. Claps, D. Dimitropoulos, V. Raghunathan, Y. Han, and B. Jalali, Observation of stimulated Raman amplification in silicon waveguides, Opt. Express **11,** 1731 (2003).

[5] R. Espinola, J. Dadap, R. Osgood, S. McNab, and Y. Vlasov, Raman amplification in ultrasmall silicon-on-insulator wire waveguides, Opt. Express **12,** 3713 (2004).

[6] A. Liu, H. Rong, M. Paniccia, O. Cohen, and D. Hak, Net optical gain in a low loss silicon-on-insulator waveguide by stimulated Raman scattering, Opt. Express **12,** 4261 (2004).

[7] Q. Xu, V. Almeida, and M. Lipson, Time-resolved study of Raman gain in highly confined silicon-on-insulator waveguides, Opt. Express **12,** 4437 (2004).

[8] O. Boyraz and B. Jalali, Demonstration of a silicon Raman laser, Opt. Express **12,** 5269 (2004).

[9] M. Krause, H. Renner, and E. Brinkmeyer, Analysis of Raman lasing characteristics in silicon-on-insulator waveguides, Opt. Express **12,** 5703 (2004).

[10] T. Liang and H. Tsang, Efficient Raman amplification in silicon-on-insulator waveguides, Appl. Phys. Lett. **85,** 3343 (2004).

[11] R. Jones, H. Rong, A. Liu, A. Fang, M. Paniccia, D. Hak, and O. Cohen, Net continuous wave optical gain in a low loss silicon-on-insulator waveguide by stimulated Raman scattering, Opt. Express **13,** 519 (2005).

[12] H. Rong, A. Liu, R. Jones, O. Cohen, D. Hak, R. Nicolaescu, A. Fang, and M. Paniccia, An all-silicon Raman laser, Nature **433,** 292 (2005).

[13] H. Rong, R. Jones, A. Liu, O. Cohen, D. Hak, A. Fang, and M. Paniccia, A continuous-wave Raman silicon laser, Nature **433,** 725 (2005).

[14] H. Rong, S. Xu, Y. Kuo, V. Sih, O. Cohen, O. Raday, and M. Paniccia, Low-threshold continuous-wave Raman silicon laser, Nat. Photonics **1,** 232 (2007).

[15] H. Rong, S. Xu, O. Cohen, O. Raday, M. Lee, V. Sih, and M. Paniccia, A cascaded silicon Raman laser, Nat. Photonics **2,** 170 (2008).

[16] Y. Takahashi, Y. Inui, M. Chihara, T. Asano, R. Terawaki, and S. Noda, A micrometre-scale Raman silicon laser with a microwatt threshold, Nature **498,** 470 (2013).

[17] Y. Takahashi, Y. Inui, M. Chihara, T. Asano, R. Terawaki, and S. Noda, High-Q resonant modes in a photonic crystal heterostructure nanocavity and applicability to a Raman silicon laser, Phys. Rev. B **88,** 235313 (2013).

[18] T. Liang and H. Tsang, Role of free carriers from two-photon absorption in Raman amplification in silicon-on-insulator waveguides, Appl. Phys. Lett. **84,** 2745 (2004).

[19] T. Liang and H. Tsang, Nonlinear absorption and Raman scattering in silicon-on-insulator optical waveguides, IEEE J. Sel. Top. Quantum. Electron. **10,** 1149 (2004).

[20] H. Rong, A. Liu, R. Nicolaescu, M. Paniccia, O. Cohen, and D. Hak, Raman gain and nonlinear optical absorption measurements in a low-loss silicon waveguide, Appl. Phys. Lett. **85,** 2196 (2004).

[21] D. Dimitropoulos, R. Jhaveri, R. Claps, J. C. S. Woo, and B. Jalali, Lifetime of photogenerated carriers in silicon-on-insulator rib waveguides, Appl. Phys. Lett. **86,** 071115 (2005).

[22] S. Noda, A. Chutinan, and M. Imada, Trapping and emission of photons by a single defect in a photonic bandgap structure, Nature **407,** 608 (2000).

[23] Y. Akahane, T. Asano, B. S. Song, and S. Noda, High-Q photonic nanocavity in a two-dimensional photonic crystal, Nature **425,** 944 (2003).

[24] B. S. Song, S. Noda, T. Asano, and Y. Akahane, Ultra-High-Q photonic double-heterostructure nanocavity, Nat. Mater. **4,** 207 (2005).

[25] M. Notomi, A. Shinya, S. Mitsugi, G. Kira, E. Kuramochi, and T. Tanabe, Optical bistable switching action of Si high-Q photonic-crystal nanocavities, Opt. Express **13,** 2678 (2005).

[26] T. Uesugi, B. S. Song, T. Asano, and S. Noda, Investigation of optical nonlinearities in an ultra-high-Q Si nanocavity in a two-dimensional photonic crystal slab, Opt. Express **14,** 377 (2006).

[27] T. Tanabe, H. Sumikura, H. Taniyama, A. Shinya, and M. Notomi, All-silicon sub-Gb/s telecom detector with low dark current and high quantum efficiency on chip, Appl. Phys. Lett. **96,** 101103 (2010).

[28] T. Tanabe, K. Nishiguchi, A. Shinya, E. Kuramochi, H. Inokawa, M. Notomi, K. Yamada, T. Tsuchizawa, T. Watanabe, H. Fukuda, H. Shinojima, and S. Itabashi, Fast all-optical switching using ion-implanted silicon photonic crystal nanocavities, Appl. Phys. Lett. **90,** 031115 (2007).

[29] M. Fujita, B. Gelloz, N. Koshida, and S. Noda, Reduction in surface recombination and enhancement of light emission in silicon photonic crystals treated by high-pressure water-vapor annealing, Appl. Phys. Lett. **97,** 121111 (2010).

[30] D. Yamashita, Y. Takahashi, T. Asano, and S. Noda, Raman shift and strain effect in high-Q photonic crystal silicon nanocavity, Opt. Express **23,** 3951 (2015).

[31] Y. Takahashi, Y. Tanaka, H. Hagino, T. Sugiya, Y. Sato, T. Asano, and S. Noda, Design and demonstration of high-Q photonic heterostructure nanocavities suitable for integration, Opt. Express **17,** 18093 (2009).

[32] T. Aasno, Y. Ochi, Y. Takahashi, K. Kishimoto, and S. Noda, Photonic crystal nanocavity with a Q factor exceeding eleven million, Opt. Express **25,** 1769 (2017).

[33] K. Ashida, M. Okano, M. Ohtsuka, M. Seki, N. Yokoyama, K. Koshino, M. Mori, T. Asano, S. Noda, and Y. Takahashi, Ultrahigh-Q photonic crystal nanocavities fabricated by CMOS process technologies, Opt. Express **25,** 18165 (2017).

[34] H. Hagino, Y. Takahashi, Y. Tanaka, T. Asano, and S. Noda, Effects of fluctuation in air hole radii and positions on optical characteristics in photonic crystal heterostructure nanocavities, Phys. Rev. B **79,** 085112 (2009).

[35] R. Konoike, H. Nakagawa, M. Nakadai, T. Asano, Y. Tanaka, and S. Noda, On-demand transfer of trapped photons on a chip, Sci. Adv. **2,** e1501690 (2016).

[36] T. Asano, B.-S. Song, and S. Noda, Analysis of the experimental Q factors (~1 million) of photonic crystal nanocavities, Opt. Express **14,** 1996 (2006).

[37] J. C. Sturm and C. M. Reaves, Silicon temperature measurement by infrared absorption. Fundamental processes and doping effects, IEEE Trans. Electron Devices **39,** 81 (1992).

[38] T. Tanabe, K. Nishiguchi, E. Kuramochi, and M. Notomi, Low power and fast electro-optic silicon modulator with

lateral p-i-n embedded photonic crystal nanocavity, Opt. Express **17,** 22505 (2009).

[39] B. Ellis, M. A. Mayer, G. Shambat, T. Sarmiento, J. Harris, E. E. Haller, and J. Vuckovic, Ultralow-threshold electrically pumped quantum-dot photonic-crystal nanocavity laser, Nat. Photon. **5,** 297 (2011).

[40] R. A. Elliott, R. K. DeFreez, T. L. Paoli, R. D. Burnham, and W. Streifer, Dynamic Characteristics of Phase-Locked Multiple Quantum Well Injection Laser, IEEE J. Quant. Electron. **21,** 598 (1985).

[41] T. Tanabe, M. Notomi, S. Mitsugi, A. Shinya, and E. Kuramochi, Fast bistable all-optical switch and memory on a silicon photonic crystal on-chip, Opt. Lett. **30,** 2575 (2005).

[42] V. Sih, S. Xu, Y.-H. Kuo, H. Rong, M. Paniccia, O. Cohen, and O. Raday, Raman amplification of 40 Gb/s data in low-loss silicon waveguides, Opt. Express **15,** 357 (2007).

[43] T. Johnson, M. Borselli, and O. Painter, Self-induced optical modulation of the transmission through a high-Q silicon microdisk resonator, Opt. Express **14,** 817 (2006).

[44] W. Pernice, M. Li, and H. Tang, Time-domain measurement of optical transport in silicon micro-ring resonators, Opt. Express **18,** 18438 (2010).

[45] H. Gibbs, *Optical Bistability: Controlling Light with Light* (Academic Press, Orlando, 1985).

[46] Y. Ooka, T. Tetsumoto, N. Daud, and T. Tanabe, Ultrasmall in-plane photonic crystal demultiplexers fabricated with photolithography, Opt. Express **25,** 1521 (2017).

[47] S. Yamada, B. S. Song, J. Upham, T. Asano, Y. Tanaka, and S. Noda, Suppression of multiple photon absorption in a SiC photonic crystal nanocavity operating at 1.55 μm, Opt. Express **20,** 14789 (2012).

[48] X. Yang and C. Wong, Coupled-mode theory for stimulated Raman scattering in high-Q/V_m silicon photonic band gap defect cavity lasers, Opt. Express **15,** 4763 (2007).

[49] X. Checoury, Z. Han, and P. Boucaud, Stimulated Raman scattering in silicon photonic crystal waveguides under continuous excitation, Phys. Rev. B **82,** 041308(R) (2010).

[50] A. Chutinan, M. Mochizuki, M. Imada, and S. Noda, Surface-emitting channel drop filters using single defects in two-dimensional photonic crystal slabs, Appl. Phys. Lett. **79,** 2690 (2001).

[51] K. H. Hellwege, O. Madelung, M. Schultz, and H. Weiss, *LANDORT-BORNSTEIN New Series 17* (Springer-Verlag, Berlin, Heidelberg, New York, 1982).

[52] G. Cocorullo, F. G. Della Corte, and I. Rendina, Temperature dependence of the thermo-optic coefficient in crystalline silicon between room temperature and 550 K at the wavelength of 1523 nm, Appl. Phys. Lett. **74,** 3338 (1999).

[53] M. Dinu, F. Quochi, and H. Garcia, Third-order nonlinearities in silicon at telecom wavelengths, Appl. Phys. Lett. **82,** 2954 (2003).